

# Oxygen evolution reaction activity of $\text{Sr}_2\text{Ta}_2\text{O}_7$ and $\text{Sr}_2\text{Nb}_2\text{O}_7$ surfaces

Maria Bouri, Nicolas Niederhauser, Benjamin Künzli, Maximilian Amsler, and  
Ulrich Aschauer\*

*Department of Chemistry, Biochemistry and Pharmaceutical Sciences, University of Bern,  
Freiestrasse 3, CH-3012 Bern, Switzerland*

E-mail: [ulrich.aschauer@unibe.ch](mailto:ulrich.aschauer@unibe.ch)

Phone: +41 31 684 56 29

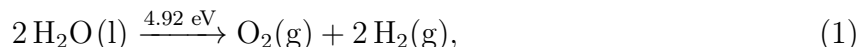
This document is the Accepted Manuscript version of a Published Work that appeared in final form in the Journal of Physical Chemistry C, copyright © 2022 American Chemical Society, after peer review and technical editing by the publisher. To access the final edited and published work see <https://doi.org/10.1021/acs.jpcc.2c00649>.

## Abstract

Oxide materials with a perovskite-derived layered structure often show better photocatalytic performance compared to non-layered materials of similar composition. Here we investigate the catalytic activity for the oxygen evolution reaction (OER) on surfaces of the layered Carpy-Galy oxides  $\text{Sr}_2\text{Ta}_2\text{O}_7$  and  $\text{Sr}_2\text{Nb}_2\text{O}_7$ . We find that the (010) surface parallel to the layering shear plane is not relevant for photocatalysis. The (100) surface perpendicular to this plane, on the other hand, can catalyze the OER, at least for  $\text{Sr}_2\text{Ta}_2\text{O}_7$ , whereas  $\text{Sr}_2\text{Nb}_2\text{O}_7$  is inactive for the OER without a cocatalyst, both in agreement with experiment. The OER activity of  $\text{Sr}_2\text{Ta}_2\text{O}_7$  (100) is, however, only retained while the surface does not assume a reconstructed stepped structure via Sr dissolution which we predict to be thermodynamically favored. Engineering  $\text{Sr}_2\text{Ta}_2\text{O}_7$  into long-lasting photoelectrodes thus has to focus on exposing (100) facets as well as preventing Sr dissolution, for example via a high Sr concentration in the electrolyte.

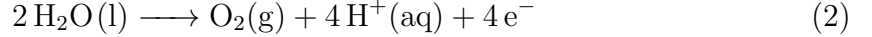
## Introduction

Renewable sources of clean energy are a key requirement to turn humanity into a sustainable society. One particularly attractive form of energy would be sunlight that is sufficiently abundant to provide 7000-8000 times our current needs<sup>1,2</sup>. Energy storage in form of batteries or fuels becomes a necessity for energy supply when the sun does not shine<sup>3</sup>. Fuels are particularly attractive for mobility applications, where hydrogen ( $\text{H}_2$ ) has attracted much attention for its high specific energy (33 kWh/kg compared to 13.9 and 12.8 kWh/kg for natural gas and petrol respectively) even though storing hydrogen still represents a challenge<sup>7</sup>.  $\text{H}_2$  can be produced from sunlight either indirectly by photovoltaics combined with an electrolyzer or directly by photocatalytic (PC) or photoelectrocatalytic (PEC) water splitting<sup>4</sup>. In both of these processes the fundamental reaction is



where the energy of  $4.92 = 4 \cdot 1.23$  eV is required for water oxidation under equilibrium conditions.

The above reaction can be separated into the oxygen (OER) and hydrogen (HER) evolution half reactions:



Of these two reactions, the OER is more demanding to catalyze as it involves four proton-coupled electron-transfer steps that limit the overall water splitting efficiency<sup>5</sup>. For photocatalysis, the efficiency of a photoanode for the OER is determined by its band gap and hence its capacity to efficiently absorb sunlight, the position of its valance and conduction band edges with respect to the water redox levels, the mobility and separability of photo-generated electrons and holes and the catalytic activity of the material surface<sup>6</sup>. The ideal catalyst has to minimize losses resulting from all these processes to exhibit a high activity.

The present work focuses on oxide photocatalysts for the OER and more specifically those with a layered perovskite-derived structure. We investigate different surfaces of  $\text{Sr}_2\text{Ta}_2\text{O}_7$  (STO, Fig. 1a) and  $\text{Sr}_2\text{Nb}_2\text{O}_7$  (SNO, Fig. 1b). These are two chemically similar oxides with the Carpy-Galy layered perovskite structure<sup>7-9</sup>. Perovskites with layered structures were shown to have higher catalytic activity than chemically similar perovskites with a non-layered structure<sup>10</sup>. Due to the lower-lying Nb  $4d$  compared to the Ta  $5d$  states, SNO has a smaller experimental band gap of 3.9 eV compared to 4.6 eV for STO<sup>11</sup>. STO was shown to have a high photocatalytic activity under UV irradiation and to produce  $\text{O}_2$  without a co-catalyst<sup>11</sup>. In contrast, SNO was shown to have a lower activity, which improved in presence of a pretreated co-catalyst<sup>11</sup>.

On surfaces of these metal-oxide the OER is usually considered to consist of four steps involving the bare surface site (\*) as well as surface bound  $\text{OH}^*$ ,  $\text{O}^*$  and  $\text{OOH}^*$  intermediate

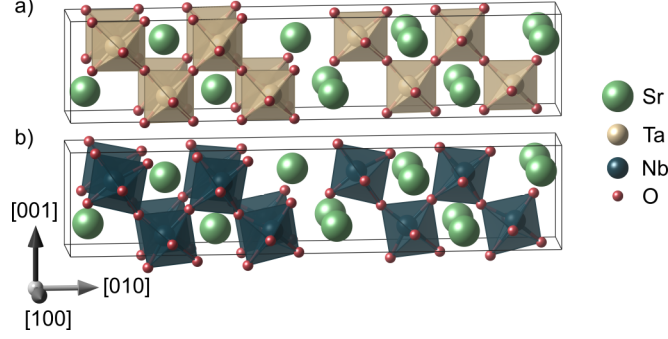
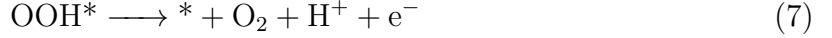
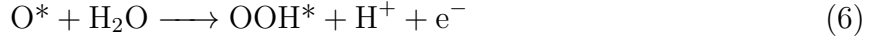


Figure 1: a)  $\text{Sr}_2\text{Ta}_2\text{O}_7$  and b)  $\text{Sr}_2\text{Nb}_2\text{O}_7$  bulk structures. The shear planes leading to the layered structure are perpendicular to  $[010]$  and located at the edge and the center of the cell.

species<sup>12–14</sup>:



The binding energies of these intermediates are not independent and in particular  $\text{OH}^*$  and  $\text{OOH}^*$  have a constant free energy difference of  $3.2 \pm 0.25 \text{ eV}^{14,15}$ . This leads to a deviation of the sum of the two steps linking these intermediates from the ideal value  $2 \cdot 1.23 = 2.46 \text{ eV}$  and hence a minimal additional energy requirement of  $0.37 \pm 0.25 \text{ eV}$  per step, referred to as the overpotential. An ideal photocatalyst will have a small overpotential and provide holes that are sufficiently energetic to overcome this overpotential. The interdependence of the intermediate energies and the fact that the OER is usually limited by either Eq. 5 or 6 allows to express the overpotential as a function of a unique descriptor, which is commonly chosen as Eq. 5<sup>12,14,16</sup>. Plotting the OER overpotential against the free energy difference of the  $\text{OH}^*$  to  $\text{O}^*$  oxidation, a volcano-shaped graph is obtained (see Results & Discussion for examples)<sup>14</sup>. Active sites on the left branch of the volcano bind  $\text{O}^*$  too strongly (and have  $\text{OOH}^*$ -formation as potential-determining step) while those on the right

branch adsorb O\* too weakly (and O\*-formation determines the potential). Close to the top of the volcano, both steps have similar magnitudes and small changes in mechanism and/or potential-determining step may be relevant<sup>17</sup>.

Our density functional theory (DFT) study predicts that the (010) surface parallel to the layering shear plane is, based on arguments of carrier mobility, catalytic activity and even surface stability not relevant for the OER. For  $\text{Sr}_2\text{Nb}_2\text{O}_7$  the overpotentials are larger than the photo-induced bias, rendering this material inactive for the OER without a cocatalyst or an additional applied potential. The  $\text{Sr}_2\text{Ta}_2\text{O}_7$  (100) surface perpendicular to this plane can photocatalyze the OER even if considering surface band bending as long as the surface remains flat and does not reconstruct into a stepped surface via Sr dissolution. Since OER activity is experimentally observed, this dissolution must be slow compared to the timescale of the OER experiments. Nevertheless our calculations show a strong thermodynamic driving force for dissolution under basic pH conditions, which we predict to eventually lead to the OER-inactive stepped surface. Our results thus predict that for long-term OER operation  $\text{Sr}_2\text{Ta}_2\text{O}_7$  photocatalysts will have to be engineered to primarily expose (001) facets as well as to prevent Sr dissolution, for example via a high Sr concentration in the electrolyte.

## Methods

Density functional theory (DFT) calculations were performed with the QUANTUM ESPRESSO package<sup>18,19</sup>, using the generalized gradient approximation (GGA) Perdew-Burke-Ernzerhof (PBE)<sup>20</sup> exchange correlation functional. More accurate bulk densities of states were also computed using the HSE06 density functional<sup>21,22</sup> using default values for the fraction of exact exchange and screening. The cutoff for the plane-wave basis was set to 35 and 40 Ry combined with augmented density cutoffs of 280 and 320 Ry respectively for SNO and STO. Ultrasoft pseudopotentials<sup>23</sup> contained Sr(4s, 4p, 4d, 5s, 5p), Ta(5s, 5p, 5d, 6s, 6p), Nb(4s, 4p, 4d, 5s, 5p), O(2s, 2p) and H(1s) valence states.

STO and SNO crystal structures were taken from Ishizawa *et al.*<sup>24,25</sup> and optimized until forces converged below 0.025 eV/Å and stresses below 0.5 kBar. Both conventional unit cells contain 44 atoms and belong to the orthorhombic space groups  $Cmcm$  for STO and  $Cmc2_1$  for SNO. Monkhorst-Pack<sup>26</sup>  $k$ -point meshes of dimension  $6 \times 2 \times 4$  were used to sample the Brillouin zone of both materials. The optimized lattice parameters are  $a = 3.97$  Å,  $b = 27.49$  Å and  $c = 5.72$  Å for STO and  $a = 3.97$  Å,  $b = 27.49$  Å and  $c = 5.72$  Å for SNO, in a good agreement with the experimental crystallographic data<sup>24,25</sup>.

The experimentally observed presence of octahedral rotations in SNO but not in STO (see Fig. 1) is surprising, given the equivalent ionic radii of Ta<sup>5+</sup> and Nb<sup>5+</sup> (both 0.64 Å in octahedral coordination)<sup>27</sup>. We verified the dynamical stability of the high symmetry STO structure using phonon calculations within the frozen phonon approach<sup>28</sup> and, as shown in the Supporting Information (SI) Section S2, found no imaginary modes. This confirms the experimentally determined structures and points to octahedral rotations in SNO being driven by the layered structure rather than tolerance factor arguments<sup>29</sup>.

Surfaces perpendicular to the [100] and [010] directions were constructed for both materials based on the optimized bulk structures. A 10 Å vacuum was used for all slabs and terminations without dipole were selected as polar surfaces have a diverging electrostatic energy and would have to undergo reconstructions<sup>30–32</sup>. In all surface calculations a dipole correction<sup>33</sup> along the surface-normal direction was added to cancel any spurious electric field in the vacuum region resulting from the adsorbates or relaxations. Reciprocal space meshes with same dimensions as for bulk calculations but reduced to a single point along the surface normal were used for slab calculations.

The (100) surfaces have 4 Ta/Nb and 4 Sr atoms as reactive sites and consist of a total of 8 atomic layers (Fig. 2a,c). Slabs are stoichiometric and the intermediate O-rich layer is perpendicular to the surface normal, leading to good charge mobility from the bulk to the surface (see electronic band structures in SI Fig. S2). The STO and SNO (100) slabs are 13.99 Å and 13.96 Å thick respectively. During structural optimization the two middle

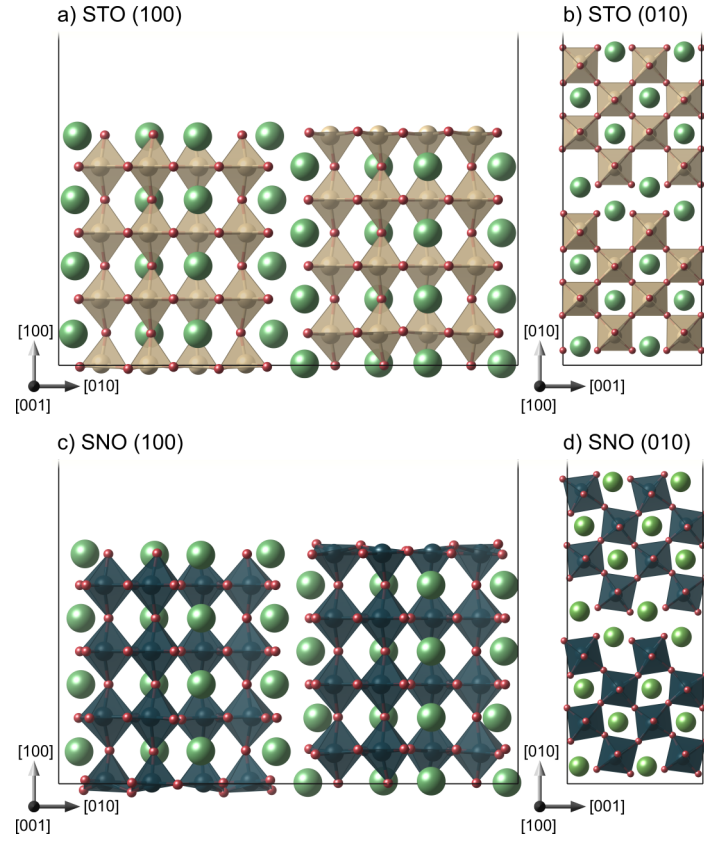


Figure 2: Side view of a)  $\text{Sr}_2\text{Ta}_2\text{O}_7$  (100), b)  $\text{Sr}_2\text{Ta}_2\text{O}_7$  (010), c)  $\text{Sr}_2\text{Nb}_2\text{O}_7$  (100) and d)  $\text{Sr}_2\text{Nb}_2\text{O}_7$  (010) surface slabs.

atomic layers were kept fixed at bulk positions, leaving the three bottom and three top atomic layers free to relax.

The (010) slabs were constructed as  $2 \times 2 \times 1$  supercells of the surface unit cells. They both have 4 Sr atoms as reactive sites and are 25.16 Å (STO) and 25.00 Å (SNO) thick, respectively (Fig. 2b,d). In this case, the O-rich layer is perpendicular to the surface normal and its Sr and O atoms were kept fixed at bulk positions.

Surface defects are also included in our analysis as A-site atoms are prone to dissolve from the surface in contact with water<sup>34,35</sup>. We thus reconstructed the (100) and (010) surfaces by removing the Sr surface atoms (both top and bottom layer) along with the same number of surface oxygen atoms to retain charge-neutral slabs. Stability of these surfaces was evaluated via the approach of Rong and Kolpak that considers formation of dissolved Sr and O species<sup>36</sup> (see SI Section S1 for details). This dissolution results in grooved (010) and stepped (100) surfaces. We note that more severe surface restructuring such as formation of an amorphous layer was not considered in this study, due to the challenge of modeling an amorphous state in periodic DFT.

To evaluate the catalytic activity of these surfaces, we follow the thermochemical approach of Nørskov *et al.*<sup>13</sup> to calculate the OER free energy diagrams and the associated overpotentials (see SI Section S1 for zero-point energies). Recombination barriers of dissociated reaction intermediates were evaluated using the climbing-image nudged-elastic band (NEB) method<sup>37</sup>, using a path convergence threshold of 0.05 eV/Å and 7 images per path.

## Results and Discussion

### Flat (100) surfaces

We compute the OER free energy profile on Ta and Nb sites of STO and SNO (100) surfaces. We predict positive values (see Table 1) for the overpotential but, as per convention, plot its negative value as a function of the free energy difference of step 2 (Eq. 5), which highlights



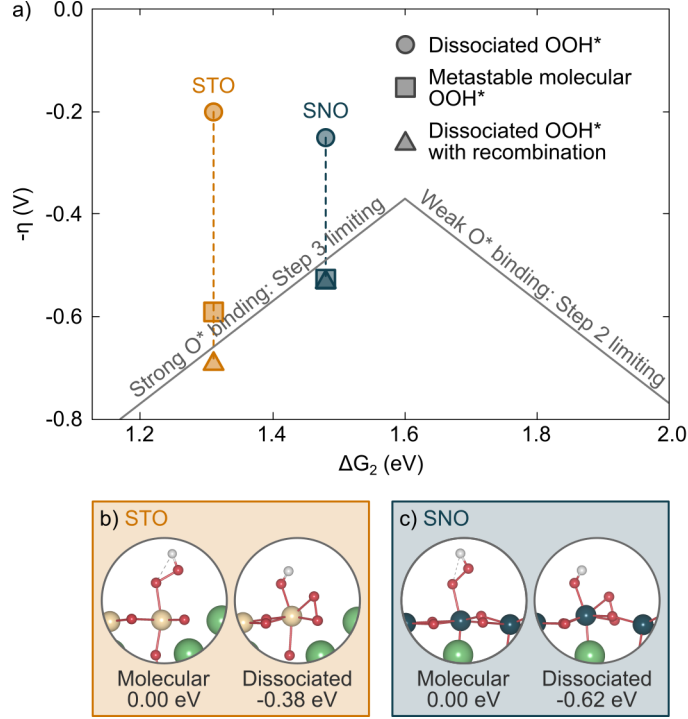


Figure 3: a) OER volcano plot of the negative overpotential ( $\eta$ ) versus the free energy change of step 2 on STO and SNO (100) surfaces. The overpotential predicted by the universal scaling relations is shown as solid lines. b) and c) show the metastable molecular and the stable dissociated OOH\* configurations for STO at the edge of the terrace and SNO within the terrace respectively.

a strong deviation of the computed overpotential from the left branch of the OER volcano (Fig. 3). The validity of the resulting very low overpotentials (0.20 V for STO and 0.25 V for SNO, see Table 1) is however questionable since we observe dissociation of the OOH\* intermediate on both surfaces (see Fig. 3b and c). For both surfaces the distance between the O and OH fragments is 2.63 Å. This dissociation lowers the energy by 0.38 eV on STO and 0.62 eV on SNO. The layer-averaged Löwdin charges for the adsorbate, surface and subsurface layers for the molecular and dissociated configuration as well as the clean STO surface (Table 2) reveal almost no charge transfer from the surface to the adsorbates and hence weak bonding for the intact OOH\*, whereas significantly more charge transfer leads to a stronger bond for the dissociated OOH\*. This stabilization of OOH\* leads to a reduction of the height of step 3 (Eq. 6) without affecting steps 1 and 2 and hence a fairly balanced OER with all steps close to 1.23 eV.

**Table 1: OER free energy steps ( $\Delta G$  in eV) and resulting overpotential ( $\eta$  in V) on SNO and STO (100) surfaces. The potential limiting step is highlighted in bold.**

Material	Mechanism	$\Delta G_1$	$\Delta G_2$	$\Delta G_3$	$\Delta G_4$	$\eta$
STO	(dissoc.)	1.03	1.31	<b>1.53</b>	1.03	0.20
STO	(metastab. molec.)	1.03	1.31	<b>1.82</b>	0.74	0.59
STO	(dissoc. recomb.)	1.03	1.31	1.43	<b>1.92</b>	0.69
SNO	(dissoc.)	1.20	<b>1.48</b>	1.14	1.08	0.25
SNO	(metastab. molec.)	1.20	1.48	<b>1.76</b>	0.45	0.53
SNO	(dissoc. recomb.)	1.20	1.48	1.11	<b>1.76</b>	0.53

**Table 2: Layer-averaged Löwdin charges (in e) of the clean STO (100) surface as well as the one with one molecular or dissociated OOH\*.**

Layer	Clean	Molecular OOH*	Dissociated OOH*
Adsorbates	-	-0.02	-0.32
Surface	0.71	0.81	1.16
Sub-surface	0.18	0.17	0.13

We can retain the undissociated OOH\* intermediate as a metastable state by placing it precisely in top position. Computing the OER free energy profile using this metastable state, does in fact lead to an agreement with the universal scaling relations and overpotentials close to the left branch of the OER volcano (Fig. 3). The overpotential, consequently, is much larger (Table 1) at 0.69 V (STO) and 0.53 V (SNO). We stress however that due to the unstable state of the undissociated OOH\*, the mechanism involving these intermediates is unlikely to occur.

In search of a realistic mechanism in presence of spontaneous OOH\* dissociation, we will consider that after the dissociation, the OH\* fragment gets oxidized followed by the recombination of the two O\* and desorption as an O<sub>2</sub> molecule<sup>17</sup>. The recombination and desorption steps are not potential but only temperature dependent. The Gibbs free energy profile of this mechanism is shown in Fig. 4. For both STO and SNO, the first two steps are the same in the mechanisms involving molecular and dissociated OOH\* and we can see that they are close to the ideal catalyst with step heights close to 1.23 eV. Differences start to appear for step 3, where the stabilization of the dissociated OOH\* lead to a near-ideal

step height for both materials. Importantly though, the oxidation in step 4, leading to two separated  $\text{O}^*$  on the surface, has a step height of 1.92 eV for STO and 1.76 eV for SNO. These are much larger than 1.23 eV and will lead to overpotentials of 0.69 V for STO and 0.53 V for SNO. These overpotentials are similar to the ones obtained using the metastable molecular  $\text{OOH}^*$  (see Table 1).

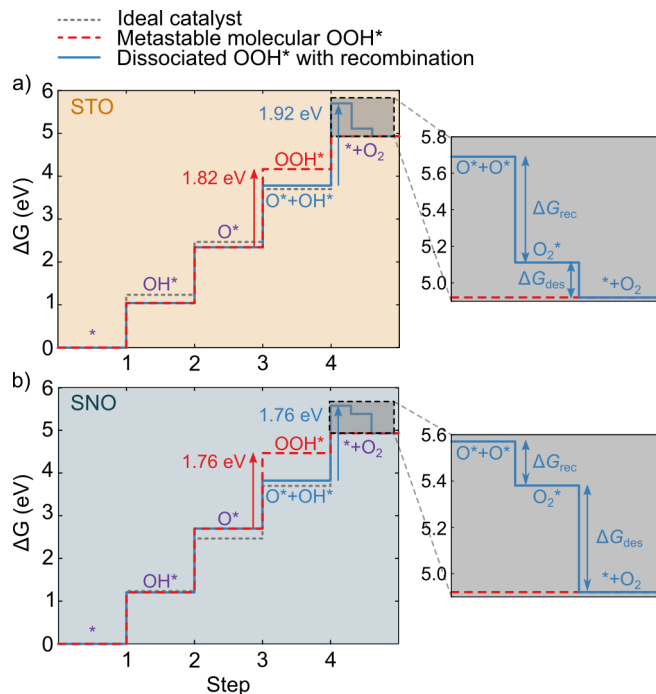


Figure 4: Gibbs free energy profile of the OER intermediates on a) the Ta site of the SNO (100) surface and b) the Nb site of the SNO (100) surface. Limiting steps are indicated by vertical arrows. The zoom-ins show the steps involving the oxidation of the second  $\text{OH}^*$  and the recombination of the two  $\text{O}^*$  and the  $\text{O}_2$  desorption.

We note that on both surfaces the recombination of the two  $\text{O}^*$  to  $\text{O}_2$  ( $G_{\text{rec}}$ ) and  $\text{O}_2$  desorption ( $G_{\text{des}}$ ) are exothermic by 0.58 and 0.18 eV for STO and 0.19 and 0.46 eV for SNO. Despite this thermodynamic driving force, recombination may be kinetically hindered as we compute barriers of 0.32 eV and 0.47 eV for STO and SNO respectively via the NEB method.

## Clean stepped (100) surfaces

We further investigate the OER on stepped (100) surfaces where Sr atoms along with an equivalent number of surface O atoms as required for charge neutrality are removed on both top and bottom surfaces. We predict the free energy of formation of these stepped surfaces using the approach by Rong and Kolpak<sup>36</sup> under both acidic (pH=0,  $\text{Sr}_2^+$  ions in solution) and basic (pH=12,  $\text{SrOH}^+$  ions in solution) conditions. As seen from the data in Table 3, the dissolution of Sr atoms is exothermic for all materials and pH, but more strongly so for the basic conditions that are more representative for typical experiments using oxide catalysts.

**Table 3: Formation free energies ( $\Delta G_f$ ) for stepped (100) surfaces under acidic (pH=0) and basic (pH=12) conditions.**

Material	$\Delta G_f$ (pH=0) [eV]	$\Delta G_f$ (pH=12) [eV]
STO	-0.48	-15.52
SNO	-3.64	-18.69

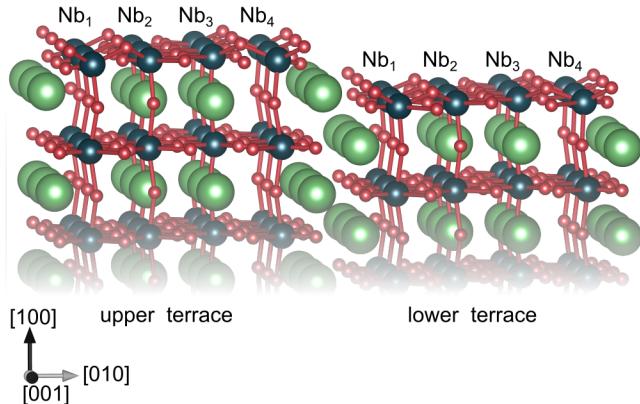


Figure 5: View of the stepped SNO (100) surface. The different sites of the upper and lower terrace are numbered in analogy to Table 4.

The (100) surface will hence be stepped under typical operation conditions. The formation of the step and the appearance of inequivalent Nb or Ta sites which are either on the upper or lower terrace as well as closer or further from the step edge (see Fig. 5 for SNO) is expected to affect the OER overpotential. We find the OOH intermediate to be stable in all cases on the stepped surface. Table 4 shows the required OER overpotentials for each site

on the upper and lower terraces of the stepped SNO and STO (100) surfaces.

**Table 4: OER free energy steps ( $\Delta G$  in eV) and resulting overpotential ( $\eta$  in V) at the different sites of the upper and lower terraces of stepped STO and SNO (100) surfaces. Sites are numbered as shown in Fig. 5 and potential limiting steps are highlighted in bold.**

Material	Terrace	Site	$\Delta G_1$	$\Delta G_2$	$\Delta G_3$	$\Delta G_4$	$\eta$
STO	Upper	Ta <sub>1</sub>	0.84	<b>2.60</b>	0.51	0.97	1.37
		Ta <sub>2</sub>	0.07	<b>2.17</b>	1.18	1.51	0.94
		Ta <sub>3</sub>	0.07	<b>2.17</b>	1.18	1.51	0.94
		Ta <sub>4</sub>	0.84	<b>2.60</b>	0.51	0.97	1.37
	Lower	Ta <sub>1</sub>	0.47	<b>2.67</b>	0.42	1.36	1.44
		Ta <sub>2</sub>	-0.12	<b>2.29</b>	1.01	1.73	1.06
		Ta <sub>3</sub>	-0.12	<b>2.29</b>	1.01	1.73	1.06
		Ta <sub>4</sub>	0.47	<b>2.67</b>	0.42	1.36	1.44
SNO	Upper	Nb <sub>1</sub>	1.60	<b>2.57</b>	0.32	0.42	1.34
		Nb <sub>2</sub>	0.92	<b>2.29</b>	0.85	0.86	1.06
		Nb <sub>3</sub>	0.92	<b>2.29</b>	0.85	0.86	1.06
		Nb <sub>4</sub>	1.60	<b>2.57</b>	0.32	0.43	1.34
	Lower	Nb <sub>1</sub>	1.20	<b>2.63</b>	0.27	0.82	1.40
		Nb <sub>2</sub>	0.71	<b>2.37</b>	0.75	1.09	1.14
		Nb <sub>3</sub>	0.70	<b>2.38</b>	0.75	1.09	1.15
		Nb <sub>4</sub>	1.20	<b>2.64</b>	0.27	0.81	1.41

We observe that the sites of the stepped STO (100) surface exhibit a symmetric behavior. The Ta<sub>1</sub> and Ta<sub>4</sub> sites closer to the step edge have equal overpotentials that are higher than those of the Ta<sub>2</sub> and Ta<sub>3</sub> sites further from the step edge. This is true for both the upper and lower terrace, indicating that the step negatively affects the OER performance of adjacent Ta sites. In addition, the potential limiting step for all sites is the oxidation of OH\* ( $\Delta G_2$ ). Overall, we see that the Ta sites on the upper terrace require lower overpotentials than the ones on the lower terrace rendering them more active for the OER.

On the other hand, we observe that the sites of the stepped SNO (100) surface lack the symmetry in overpotentials observed for STO. This could, apart from numerical noise, be due to the octahedral rotations, which are present for SNO but not STO (see Fig. 2) that result in different Nb-O bonding geometries and therefore in unequal binding energies for adsorbates at different Nb sites. Like for the stepped STO surface, sites at the center of

each terrace require lower overpotentials than those in proximity of the step, while also for SNO the upper terrace is more reactive than the lower terrace. Overall the stepped STO surface (lowest overpotential 0.94 V) is more active for the OER compared to the stepped SNO surface (lowest overpotential 1.06 V).

## Adsorbate-covered (100) surfaces

To determine the surface coverage under operation conditions, we define the photo-induced bias potential as the energy difference between the valence band edge and the normal hydrogen electrode (NHE). This is computed via the empirical formula<sup>38–40</sup>

$$E_{\text{VB,CB}} = E_0 + (\chi_{\text{Sr}}^2 \chi_{\text{Nb/Ta}}^2 \chi_{\text{O}}^7)^{1/11} \pm E_{\text{gap}}/2 \quad (8)$$

using the position of the NHE vs. the vacuum level ( $E_0 = -4.5$  eV), atomic Mulliken electronegativities ( $\chi_i$ ) and HSE06 band gaps ( $E_{\text{gap}}$ ). Since surface band edges can significantly deviate from the bulk band edges, we also determined the offset of the surface valence band edge compared to the one in the bulk by aligning surface and bulk PBE densities of states at a Sr 4s semi-core state<sup>41</sup>. As shown in Fig. 6a) and b) the surface valence-band edges lie more than 1 eV above the bulk band edges, more markedly so for STO than for SNO. We also find that the stepped surface generally has a higher valence band edge compared to the flat surface. We rationalize this with a strong localization of these states onto only the upper terrace that goes in hand with an increased kinetic energy. Using the HSE06 band gaps (4.45 eV for STO and 4.32 for SNO) and considering these additional surface effects, we obtain bias potentials of 1.51 and 0.55 eV for flat and stepped STO respectively, and 2.02 and 1.80 eV for flat and stepped SNO respectively. We note that the HSE06 band gap for STO agrees much better with the experimental value (4.6 eV) than for SNO (3.9 eV). In view of the limited experimental data, it is not clear if DFT overestimates the SNO band gap and what possible reasons could be. Nevertheless, we note that too large a band gap

could have artificially lowered the SNO valence band position and hence overestimated the predicted bias potential.

Using surface Pourbaix diagrams, we next predict the adsorbate coverage of these surfaces as a function of the bias potential<sup>13</sup>. Considering only pure OH and O coverages, the results shown in Fig. 6c)-f) demonstrate that, as expected, all surfaces will first assume a coverage with OH followed by a O coverage at higher bias. We note that considering mixed adsorbate layers would likely lead to smoother transitions from the clean to the OH and ultimately the O covered surface. Comparing with the predicted photo-induced biases shown as dashed vertical lines, the flat STO and stepped SNO surfaces will be OH covered, while the flat SNO surface is O covered and the stepped STO surface remains free from adsorbates. We note at this point that the low bias, resulting from high-lying surface valence-band states, renders the stepped STO surface inactive for photocatalytic water splitting, since the bias is below the equilibrium potential of 1.23 eV.

Finally, we compute the OER free energy profiles on the all adsorbate covered surfaces stable under the photo-induced bias. We exclude the stepped STO surface as it is not able to drive the OER. We also restrict ourselves to symmetry inequivalent sites and neglect the small energetic differences induced by octahedral rotation in SNO. From the data shown in Table 5 and summarized in form of volcano plots in Fig. 7 we see that all adsorbate covered surfaces fall onto the left branch of the volcano and are limited by strong binding of the \*O intermediate. The clean stepped surfaces on the other hand nicely fall on the right branch of the volcano and are limited by weak binding of the \*O intermediate. Also, sites on the upper terrace are systematically more reactive than equivalent sites on the lower terrace and central sites (2 and 3) are significantly more active than sites next to the step (1 and 4). Somewhat surprisingly, most sites on the adsorbate covered surfaces do not follow the universal scaling relations as either step 1 or 4 limits the potential. Due to these deviations from the scaling relations, we, notably, predict a very small overpotential of 0.48 V on the central site of the flat OH-covered STO (100) surface, which is however still larger than the

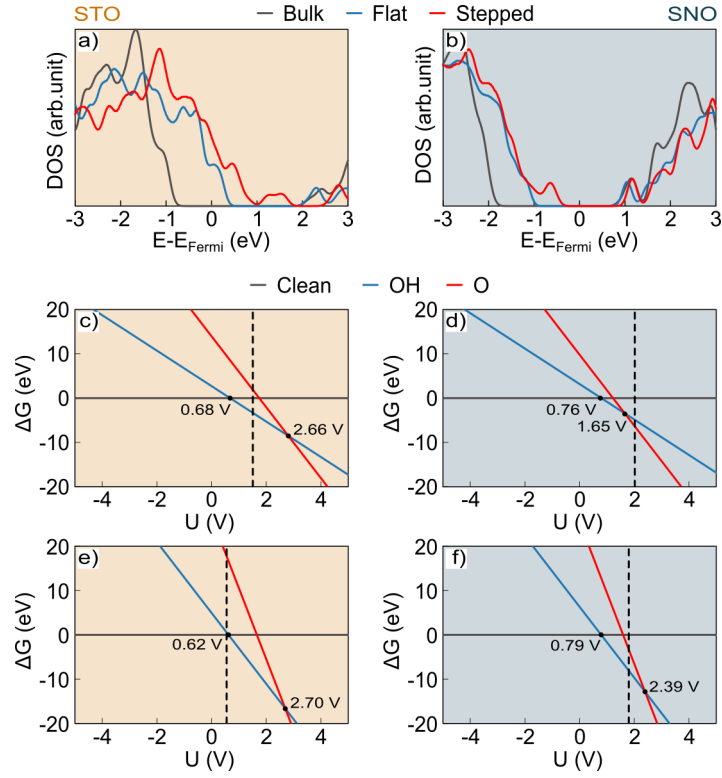


Figure 6: a) Electronic density of states of bulk as well as flat and stepped a) STO and b) SNO (100) surfaces. Surface Pourbaix diagrams for c) flat STO, d) flat SNO, d) stepped STO and f) stepped SNO (100) surfaces.



photo-induced bias (1.51 eV) minus the equilibrium potential. All other sites on adsorbate covered STO and SNO (100) surfaces have overpotentials in excess of 1.0 eV, for which even the large photo-induced biases for SNO are too small.

**Table 5: OER free energy steps ( $\Delta G$  in eV) and resulting overpotential ( $\eta$  in V) at the different sites of the adsorbate-covered STO and SNO (100) surfaces. Sites are numbered as shown in Fig. 5 and potential limiting steps are highlighted in bold.**

Material	Ads.	Terrace	Site	$\Delta G_1$	$\Delta G_2$	$\Delta G_3$	$\Delta G_4$	$\eta$
STO	OH	Flat	Ta <sub>2,3</sub>	1.40	0.55	1.25	<b>1.71</b>	0.48
			Ta <sub>1,4</sub>	<b>2.35</b>	0.08	0.92	1.57	1.12
SNO	O	Flat	Nb <sub>2,3</sub>	0.71	0.86	0.92	<b>2.43</b>	1.20
			Nb <sub>1,4</sub>	0.66	1.14	<b>2.71</b>	0.41	1.48
	OH	Upper	Nb <sub>2,3</sub>	<b>2.58</b>	0.57	0.72	1.06	1.35
			Nb <sub>1,4</sub>	<b>2.57</b>	0.15	0.50	1.70	1.34
		Lower	Nb <sub>2,3</sub>	<b>2.59</b>	0.46	0.82	1.05	1.36
			Nb <sub>1,4</sub>	<b>2.60</b>	0.23	0.66	1.43	1.37

These results indicate that STO is photocatalytically more active than SNO, which agrees with experiment<sup>11</sup>. STO’s OER activity, will, in practice, however be hampered by the fact that Sr ions are predicted to dissolve from the (100) surface and the too small bias due to the presence of surface states. A possible explanation for the experimentally observed OER activity of STO under UV irradiation could hence be that Sr dissolution is slower than the time scale of OER experiments or an involvement of carriers before phonon-mediated relaxation to the band edge<sup>42</sup>, which could occur due to the high mobility perpendicular to the (100) surface (see Fig. S2).

## (010) surfaces

We also investigate the OER activity of clean STO and SNO (010) surfaces which are both SrO-terminated and the OER hence takes place on Sr atoms. We observe that as opposed to the (100) surfaces, molecular OOH\* is stable on the Sr site compared to dissociated fragments. Therefore we consider the conventional mechanism and we find the potential limiting step for both STO and SNO surfaces to be step 1 (OH\* oxidation) with the SNO

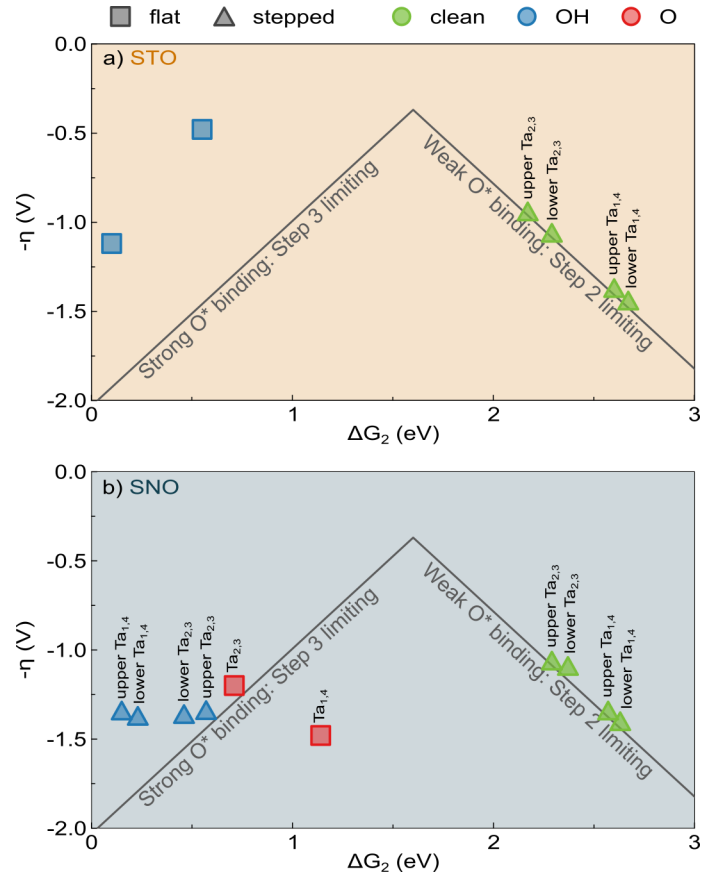


Figure 7: Volcano plots for stepped and/or adsorbate covered a) STO and b) SNO (100) surfaces.

(010) surface requiring a higher overpotential (1.07 V) than the STO (010) surface (0.61 V). Since step 1 is limiting, both the STO and SNO (010) surfaces do not agree with the universal scaling relations (see SI Fig. S3a).

We further investigate if the (010) surfaces will also undergo reconstruction as a result of Sr dissolution. We adopt a grooved surface structure in which Sr along with adjacent O have been removed (see SI Fig. S3b). As opposed to the (100) surface, we find this not to be favorable under acidic conditions (+2.08 and +1.19 eV for STO and SNO respectively), while dissolution is still exothermic under basic conditions (-5.45 eV and -6.33 eV for STO and SNO respectively), however less so than for the (100) surfaces. When computing the OER on the newly exposed Ta/Nb sites on these surfaces, we find the surfaces to be highly unstable, undergoing significant atomic rearrangement in the surface layer, in particular upon adsorption of the OOH adsorbate. While (010) surfaces are thus likely to reconstruct under operation conditions, the exact structure of the surface layer remains unclear and could even be disordered. In addition to this instability, the low carrier mobility along the surface normal (see Fig. S2), also renders this surface not very relevant for photocatalysis.

## Conclusions

We investigated the oxygen evolution reaction (OER) activity of (100) and (010) surface of the two layered Carpy-Galy oxides  $\text{Sr}_2\text{Ta}_2\text{O}_7$  (STO) and  $\text{Sr}_2\text{Nb}_2\text{O}_7$  (SNO). The (010) surface is, due to carrier mobility, catalytic activity and surface stability considerations shown not to be relevant for photocatalysis. On the clean and flat (100) surface, we predict spontaneous dissociation of the  $^*\text{OOH}$  intermediate and consider an alternative mechanism involving recombination of two  $^*\text{O}$  fragments. Using this mechanism we obtain, in disagreement with experiment, a higher activity for the flat SNO than the flat STO surface.

However, since Sr is known to fairly easily dissolve from oxide surfaces, we also consider a stepped (100) surface model with Sr and O atoms removed, which we predict to spon-

taneously form under experimentally relevant basic pH conditions. For these surfaces, we predict a higher activity for STO compared to SNO. This trend is retained also in presence of OH and O adsorbates. In presence of adsorbates, we, moreover, predict a very small overpotential for the flat STO (100) surface. The stepped STO (100) surface resulting from Sr dissolution, is, due to high-lying surfaces states, inactive for the OER. This points to the fact that STO can only be long-term active for the OER if Sr dissolution can be prevented, for example via a high Sr concentration in the electrolyte.

## Supporting Information Available

Additional method details, STO phonon band structure, electronic band structures, (010) surface data.

## Acknowledgement

This research was funded by the SNF Professorship Grants PP00P2\_157615 and PP00P2\_187185. Calculations were performed on UBELIX (<http://www.id.unibe.ch/hpc>), the HPC cluster at the University of Bern, the Swiss National Supercomputing Centre (CSCS) under projects s766, s955 and s1033 and SuperMUC at GCS@LRZ, Germany, for which we acknowledge PRACE for awarding us access.

## References

- (1) Lewis, N. S.; Nocera, D. G. Powering the planet: Chemical challenges in solar energy utilization. *Proc. Natl. Acad. Sci. U.S.A.* **2006**, *103*, 15729–15735.
- (2) Breeze, P. *Power generation technologies*; Newnes: Oxford, United Kingdom.

- (3) Hou, Y.; Vidu, R.; Stroeve, P. Solar energy storage methods. *Ind. Eng. Chem. Res.* **2011**, *50*, 8954–8964.
- (4) Nazir, H.; Louis, C.; Jose, S.; Prakash, J.; Muthuswamy, N.; Buan, M. E. M.; Flox, C.; Chavan, S.; Shi, X.; Kauranen, P. et al. Is the H<sub>2</sub> economy realizable in the foreseeable future? Part I: H<sub>2</sub> production methods. *Int. J. Hydrog. Energy* **2020**, *45*, 13777–13788.
- (5) Greeley, J.; Markovic, N. M. The road from animal electricity to green energy: combining experiment and theory in electrocatalysis. *Energy Environ. Sci.* **2012**, *5*, 9246–9256.
- (6) Takanabe, K. Photocatalytic water splitting: Quantitative approaches toward photocatalyst by design. *ACS Catal.* **2017**, *7*, 8006–8022.
- (7) Carpy, A.; Amestoy, P.; Galy, J. Contribution à l'étude du pyroniobate de calcium Ca<sub>2</sub>Nb<sub>2</sub>O<sub>7</sub>. *C.R. Acad. Sci. Paris* **1972**, *275C*, 833.
- (8) Carpy, A.; Amestoy, P.; Galy, J. Système Ca<sub>2</sub>Nb<sub>2</sub>O<sub>7</sub>-NaNbO<sub>3</sub>: synthèse et étude radiocristallographique de membres de la série AnBnX<sub>3n+2</sub> (n = 4, 5, 6). *C.R. Acad. Sci. Paris* **1973**, *277C*, 501.
- (9) Valdez, M. N.; Spaldin, N. A. Origin and evolution of ferroelectricity in the layered rare-earth-titanate, R<sub>2</sub>Ti<sub>2</sub>O<sub>7</sub>, Carpy-Galy phases. *Polyhedron* **2019**, *171*, 181–192.
- (10) Kudo, A.; Miseki, Y. Heterogeneous photocatalyst materials for water splitting. *Chem. Soc. Rev.* **2009**, *38*, 253–278.
- (11) Kudo, A.; Kato, H.; Nakagawa, S. Water splitting into H<sub>2</sub> and O<sub>2</sub> on new Sr<sub>2</sub>M<sub>2</sub>O<sub>7</sub> (M = Nb and Ta) photocatalysts with layered perovskite structures: Factors affecting the photocatalytic activity. *J. Phys. Chem. B* **2000**, *104*, 571–575.
- (12) Rossmeisl, J.; Qu, Z.-W.; Zhu, H.; Kroes, G.-J.; Nørskov, J. K. Electrolysis of water on oxide surfaces. *J. Electroanal. Chem.* **2007**, *607*, 83–89.

- (13) Valdes, A.; Qu, Z.-W.; Kroes, G.-J.; Rossmeisl, J.; Nørskov, J. K. Oxidation and photo-oxidation of water on TiO<sub>2</sub> surface. *J. Phys. Chem. C* **2008**, *112*, 9872–9879.
- (14) Man, I. C.; Su, H.-Y.; Calle-Vallejo, F.; Hansen, H. A.; Martínez, J. I.; Inoglu, N. G.; Kitchin, J.; Jaramillo, T. F.; Nørskov, J. K.; Rossmeisl, J. Universality in oxygen evolution electrocatalysis on oxide surfaces. *ChemCatChem* **2011**, *3*, 1159–1165.
- (15) Koper, M. T. Theory of multiple proton–electron transfer reactions and its implications for electrocatalysis. *Chem. Sci.* **2013**, *4*, 2710–2723.
- (16) Montoya, J. H.; Garcia-Mota, M.; Nørskov, J. K.; Vojvodic, A. Theoretical evaluation of the surface electrochemistry of perovskites with promising photon absorption properties for solar water splitting. *Phys. Chem. Chem. Phys.* **2015**, *17*, 2634–2640.
- (17) Valdes, A.; Brillet, J.; Grätzel, M.; Gudmundsdottir, H.; Hansen, H. A.; Jonsson, H.; Klüpfel, P.; Kroes, G.-J.; Le Formal, F.; Man, I. C. et al. Solar hydrogen production with semiconductor metal oxides: new directions in experiment and theory. *Phys. Chem. Chem. Phys.* **2012**, *14*, 49–70.
- (18) Giannozzi, P.; Baroni, S.; Bonini, N.; Calandra, M.; Car, R.; Cavazzoni, C.; Ceresoli, D.; Chiarotti, G. L.; Cococcioni, M.; Dabo, I. et al. QUANTUM ESPRESSO: a modular and open-source software project for quantum simulations of materials. *J. Phys. Condens. Matter* **2009**, *21*, 395502.
- (19) Giannozzi, P.; Andreussi, O.; Brumme, T.; Bunau, O.; Nardelli, M. B.; Calandra, M.; Car, R.; Cavazzoni, C.; Ceresoli, D.; Cococcioni, M. et al. Advanced capabilities for materials modelling with QUANTUM ESPRESSO. *J. Phys. Condens. Matter* **2017**, *29*, 465901.
- (20) Perdew, J. P.; Burke, K.; Ernzerhof, M. Generalized gradient approximation made simple. *Phys. Rev. Lett.* **1996**, *77*, 3865.

- (21) Heyd, J.; Scuseria, G. E.; Ernzerhof, M. Hybrid functionals based on a screened Coulomb potential. *J. Chem. Phys.* **2003**, *118*, 8207.
- (22) Heyd, J.; Scuseria, G. E.; Ernzerhof, M. Erratum: Hybrid functionals based on a screened Coulomb potential [J. Chem. Phys. 118, 8207 (2003)]. *J. Chem. Phys.* **2006**, *124*, 219906 2.
- (23) Vanderbilt, D. Soft self-consistent pseudopotentials in a generalized eigenvalue formalism. *Phys. Rev. B* **1990**, *41*, 7892.
- (24) Ishizawa, N.; Marumo, F.; Kawamura, T.; Kimura, M. The crystal structure of  $\text{Sr}_2\text{Nb}_2\text{O}_7$ , a compound with perovskite-type slabs. *Acta Crystallogr. B* **1975**, *31*, 1912–1915.
- (25) Ishizawa, N.; Marumo, F.; Kawamura, T.; Kimura, M. Compounds with perovskite-type slabs. II. The crystal structure of  $\text{Sr}_2\text{Ta}_2\text{O}_7$ . *Acta Crystallogr. B* **1976**, *32*, 2564–2566.
- (26) Monkhorst, H. J.; Pack, J. D. Special points for Brillouin-zone integrations. *Phys. Rev. B* **1976**, *13*, 5188.
- (27) Shannon, R. D. Revised effective ionic radii and systematic studies of interatomic distances in halides and chalcogenides. *Acta Crystallogr. A* **1976**, *32*, 751–767.
- (28) Togo, A.; Oba, F.; Tanaka, I. First-principles calculations of the ferroelastic transition between rutile-type and  $\text{CaCl}_2$ -type  $\text{SiO}_2$  at high pressures. *Phys. Rev. B* **2008-10**, *78*, 134106.
- (29) Goldschmidt, V. M. Die Gesetze der Krystallochemie. *Naturwissenschaften* **1926**, *14*, 477–485.
- (30) Tasker, P. W. The stability of ionic crystal surfaces. *J. Phys. C: Sol. State Phys.* **2001**, *12*, 4977.

- (31) Noguera, C. Polar oxide surfaces. *J. Phys. Condens. Matter* **2000**, *12*, R367–R410.
- (32) Goniakowski, J.; Noguera, C. Conditions for electronic reconstruction at stoichiometric polar/polar interfaces. *J. Phys. Condens. Matter* **2014**, *26*, 485010.
- (33) Bengtsson, L. Dipole correction for surface supercell calculations. *Phys. Rev. B* **1999**, *59*, 12301.
- (34) Halwidl, D.; Stöger, B.; Mayr-Schmölzer, W.; Pavelec, J.; Fobes, D.; Peng, J.; Mao, Z.; Parkinson, G. S.; Schmid, M.; Mittendorfer, F. et al. Adsorption of water at the SrO surface of ruthenates. *Nat. Mater.* **2015**, *15*, 450–455.
- (35) Akbay, T.; Staykov, A.; Druce, J.; Téllez, H.; Ishihara, T.; Kilner, J. A. The interaction of molecular oxygen on LaO terminated surfaces of  $\text{La}_2\text{NiO}_4$ . *J. Mat. Chem. A* **2016**, *4*, 13113–13124.
- (36) Rong, X.; Kolpak, A. M. Ab initio approach for prediction of oxide surface structure, stoichiometry, and electrocatalytic activity in aqueous solution. *J. Phys. Chem. Lett.* **2015**, *6*, 1785–1789.
- (37) Henkelman, G.; Uberuaga, B. P.; Jónsson, H. Climbing image nudged elastic band method for finding saddle points and minimum energy paths. *J. Chem. Phys.* **2000**, *113*, 9901–9904.
- (38) Butler, M. A.; Ginley, D. S. Prediction of flatband potentials at semiconductor-electrolyte interfaces from atomic electronegativities. *J. Electrochem. Soc.* **1978**, *125*, 228–232.
- (39) Xu, Y.; Schoonen, M. A. A. The absolute energy positions of conduction and valence bands of selected semiconducting minerals. *Am. Mineral.* **2000**, *85*, 543–556.
- (40) Castelli, I. E.; García-Lastra, J. M.; Hüser, F.; Thygesen, K. S.; Jacobsen, K. W.



Stability and bandgaps of layered perovskites for one- and two-photon water splitting. *New J. Phys.* **2013**, *15*, 105026.

- (41) Bouri, M.; Aschauer, U. Suitability of different  $\text{Sr}_2\text{TaO}_3\text{N}$  surface orientations for photocatalytic water oxidation. *Chem. Mater.* **2020**, *32*, 75–84.
- (42) Burns, E.; Aschauer, U.; Döbeli, M.; Schneider, C. W.; Pergolesi, D.; Lippert, T.  $\text{LaTiO}_2\text{N}$  crystallographic orientation control significantly increases visible-light induced charge extraction. *J. Mater. Chem. A* **2020**, *8*, 22867–22873.

## TOC Graphic

